

Gamma-Ray Burst at the extreme: “the naked-eye burst” GRB 080319B

P. R. Woźniak, W. T. Vestrand, A. D. Panaitescu, J. A. Wren, H. R. Davis, & R. R. White

*Los Alamos National Laboratory, MS-D466, Los Alamos, NM 87545
email: (wozniak, vestrand, alin, jwren, hdavis, rwhite)@lanl.gov*

ABSTRACT

On 19 March 2008, the northern sky was the stage of a spectacular optical transient that for a few seconds remained visible to the naked eye. The transient was associated with GRB 080319B, a gamma-ray burst at a luminosity distance of about 6 Gpc (standard cosmology), making it the most luminous optical object ever recorded by human kind. We present comprehensive sky monitoring and multi-color optical follow-up observations of GRB 080319B collected by the RAPTOR telescope network covering the development of the explosion and the afterglow before, during, and after the burst. The extremely bright prompt optical emission revealed features that are normally not detectable. The optical and gamma-ray variability during the explosion are correlated, but the optical flux is much greater than can be reconciled with single emission mechanism and a flat gamma-ray spectrum. This extreme optical behavior is best understood as synchrotron self-Compton model (SSC). After a gradual onset of the gamma-ray emission, there is an abrupt rise of the prompt optical flux suggesting that variable self-absorption dominates the early optical light curve. Our simultaneous multi-color optical light curves following the flash show spectral evolution consistent with a rapidly decaying red component due to large angle emission and the emergence of a blue forward shock component from interaction with the surrounding environment. While providing little support for the reverse shock that dominates the early afterglow, these observations strengthen the case for the universal role of the SSC mechanism in generating gamma-ray bursts.

Subject headings: gamma rays: bursts – cosmology: observations – shock waves

1. Introduction

The current theoretical picture of the gamma-ray burst (GRB) phenomenon involves a collapse of a massive, rotating star at the end of its normal evolution, leading to the formation of a black hole (e.g. Woosley & Bloom 2006). In the standard expanding fireball

model of GRBs part of the collapsar energy is channeled into a narrow ultra-relativistic jet with a few degree opening angle and accelerated to Lorentz factor ~ 100 – 1000 (e.g. Zhang, Woosley & MacFadyen 2003). The progress in understanding the detailed geometry and energetics of the explosion has been greatly stimulated by the launch of the Swift satellite (Gehrels et al. 2004) in the fall of 2004. High precision rapid localizations from the BAT instrument (c.f. Sakamoto et al. 2008) combined with new developments in fast optical follow-up and wide field monitoring technology (Akerlof et al. 2003; Boer 2004; Covino et al. 2004; Guidorzi et al. 2006; Perez-Ramirez, Park, & Williams 2004; Reichart et al. 2005; Vestrand et al. 2002; Beskin et al. 2008) have enabled routine observations of the early optical afterglow emission thought to arise in the external shock from the interaction of the jet with the circum-burst medium. In a few bursts it was possible to detect the prompt optical emission from internal shocks within the jet. (e.g. Blustin et al. 2006; Vestrand et al. 2005, 2006; Rykoff et al. 2005).

The intrinsic luminosity of GRBs spans several orders of magnitude, and studying the extreme cases provides a handle on the source of this diversity. The optical transient associated with GRB 080319B set a new record of both the apparent magnitude and the intrinsic luminosity. For a few seconds it was detectable with the unaided eye from a dark sky site. More importantly, new generation optical sky sentinels and rapid response telescopes were able to measure—over an unprecedented range of brightness—the development of the explosion and the afterglow in the minutes before, during, and after the stellar collapse. Sampling the broad-band spectral evolution of GRBs and their afterglows with high-cadence, multi-wavelength light curves reaching into the critical first minutes of the explosion is crucial to understanding the emission mechanism. Here we present comprehensive sky monitoring and multi-color optical follow-up observations of GRB 080319B collected by the RAPTOR telescope network.

2. Observations

On March 19, 2008, at 06:12:49 Universal Time (UT) the Burst Alert Telescope (BAT) onboard the Swift satellite (Gehrels et al. 2004) was triggered by an intense pulse of gamma rays from GRB 080319B (Racusin et al. 2008a). The BAT localization distributed over the Gamma-Ray Burst Coordinate Network (GCN) at 06:12:56 UT was received by the RAPTOR telescope network within a second, while the follow-up response for the previous alert (GRB 080319A) was still in progress. The system owned by the Los Alamos National Laboratory is located at the Fenton Hill Observatory at an altitude of 2,500 m (Jemez Mountains, New Mexico). RAPTOR-Q is a continuous all sky monitor with the approximate magnitude

limit 9.5 (unfiltered R -band equivalent, C_R). RAPTOR-P is an array of four 200-mm Canon telephoto lenses, each covering a field of view 8×8 square degrees down to $C_R \sim 15$ mag, normally used to patrol large areas of the sky for optical flashes. RAPTOR-T instrument consists of four co-aligned 0.4-m telescopes on a single fast-slewing mount and provides simultaneous images in four photometric bands (V , R , I and clear). Both rapidly slewing telescopes available on the network, RAPTOR-P and T, responded in the override mode upon receiving the X-ray Telescope (XRT) localization at 06:13:16 UT with the first follow-up exposure starting at 06:13:24 UT (35 s after the BAT trigger). Independently of the follow-up observations, the burst location was covered by our continuous all-sky monitor RAPTOR-Q. Those measurements rule out the presence of optical precursor for 30 minutes prior to the gamma-ray burst down to a flux limit of 0.5 Jy (3σ) or just 2.5% of the peak flux. Unfiltered RAPTOR-Q and P magnitudes were calibrated using several hundred stars from the Northern Sky Variability Survey (NSVS; Woźniak et al. (2004)). The color terms and absolute calibration for RAPTOR-T measurements were obtained with 1–2 dozen stars per filter using secondary field standards from Henden (2008). Observations were collected in sub-optimal weather with wind-shake affecting about 50% of RAPTOR-T measurements. The early non-detections in RAPTOR-T data are due to saturation. Photometric measurements after $t = 2200$ s are based on co-added images utilizing between 5 and 20 individual exposures. The combined error bars are photon noise estimates with the systematic uncertainty of 0.02 mag added in quadrature.

3. Results

The light curve resulting from our coordinated measurements (Fig. 1, Table 2) shows the optical flash that within several seconds of the onset reached a peak visual magnitude ~ 5.3 . At red-shift $z = 0.937$ (Vreeswijk et al. 2008) and assuming standard cosmology ($\Omega_m = 0.27, \Omega_\Lambda = 0.73, H_0 = 71$ km/s) this corresponds to absolute magnitude $M_V \simeq -38.6$ breaking the previous luminosity record held by GRB 990123 by nearly an order of magnitude. The simultaneous multi-color measurements recorded by RAPTOR-T starting at $t \simeq 100$ s (Figs. 2 and 3) reveal an afterglow light curve with a very steep initial decline ($\alpha_1 \sim 2.5$), modulated by several small bumps, and followed by a gradual transition to a slower decay after 800–1000 s with $\alpha_2 \sim 1.2$. The transition is accompanied by a change in color $\Delta(V - I) \simeq -0.25$ mag that is largely a result of mixing between two components with colors that are approximately constant. These trends agree with other published data on GRB 080319B from PAIRITEL, KAIT, Nickel, UVOT, and Gemini-S instruments (Bloom et al. 2008). Racusin et al. (2008c) presented an extensive broad-band study of GRB 080319B based on several independent data sets. All available data sets are consistent within the

quoted uncertainties. In our joined model fits (Fig. 3 and Table 1) we included the data from Bloom et al. (2008) in order to constrain the host galaxy reddening and late time decay rate. We adopted a double power-law model with SMC-like extinction (Pei 1992) and spectral index β_1, β_2 for the red and blue components with decay rates α_1, α_2 that dominate, correspondingly, early and late times. There is only a modest amount of dust in the host galaxy reference frame, $A_V \simeq 0.06$ mag, and the Galactic extinction $E_{B-V} = 0.01$ is negligible (Schlegel, Finkbeiner & Davis 1998). While the model with constant intrinsic spectral slopes provides an acceptable fit to the data, the afterglow becomes redder again after $\sim 10^4$ s. Adding a third power-law results in a degenerate fit, but we can approximately assess the effect of the additional component by adding a time dependent spectral slope β_2 with linear dependence on $\log t$ that significantly improves the fit (Table 1).

4. Discussion

4.1. Prompt optical emission

The variations of the optical emission during the burst roughly follow the onset, the three major peaks, and the final decline of the gamma-ray flux (Fig. 2), indicating that both types of radiation have a closely linked source. In the standard fireball model (Meszaros & Rees 1993; Waxman 1997), this prompt emission is generated in internal shocks due to colliding shells of material moving at different bulk Lorentz factors within the ultra-relativistic outflow. From the burst spectrum measured by Konus satellite (Golenetskii et al. 2008) we find the gamma-ray flux density ~ 7 mJy near the peak at 650 keV. The flux density observed in the optical band in the same time interval is ~ 10 Jy and falls four orders of magnitude above the extrapolation of the low-energy gamma-ray spectrum ($F \propto \nu^{0.18 \pm 0.01}$). The most natural scenario that accommodates the presence of these two distinct spectral components is a synchrotron self-Compton (SSC) model, in which optical photons are generated as synchrotron emission and gamma rays are a result of inverse-Compton scatterings of those photons to higher energies. Both processes operate simultaneously in the power-law distribution of electrons accelerated by the shock front, producing a tracking behavior between the low-energy synchrotron hump and its high-energy ‘‘Compton image’’. The apparent degree of correlation between the gamma-ray and optical light curves can vary widely due to several factors such as the presence of the early afterglow emission, the effective width of the energy distribution of scattering electrons, and the location of the compared frequency ranges within the double peaked SSC spectrum. Above the peak frequency, a typical synchrotron spectrum decreases sharply as $\sim \nu^{-p/2}$ with $p \sim 3$, sometimes faster, if the corresponding electrons cannot cool effectively (Panaitescu & Kumar 2007). Therefore,

the observed prompt optical flux and its ratio to gamma-ray flux will be very sensitive to the location of the synchrotron peak, especially if most of the low frequency $\nu^{1/3}$ shoulder is self-absorbed. The extraordinary brightness of the prompt optical emission in GRB 080319B can then be understood as a result of fortuitous positioning of the synchrotron peak in the optical band.

The rise of the prompt optical emission to its peak flux at $t \sim 18$ s is somewhat delayed and extremely steep by comparison with the onset of the gamma-ray emission. We find $F \propto t^\alpha$ with $\alpha_{\text{opt}} = 3.08 \pm 0.20$ for TORTORA light curve and $\alpha_\gamma \simeq 1/3$ observed by BAT, so even after scaling by the gamma-ray emission the optical flux rises as $\sim t^3$ prior to the first peak (Fig. 2). This suggests that at the beginning of the burst $\nu_{\text{opt}} < \nu_a$, i.e. the optical frequency is below the self-absorption cut-off of the synchrotron radiating fluid. Assuming that the emitting shell of shocked material in the relativistic outflow expands and cools adiabatically, we can estimate the evolution of the electron Lorentz factor $\gamma_e \propto t^{-1}$ and magnetic field $B \propto t^{-2}$ with constant number of electrons N_e and bulk Lorentz factor Γ . The synchrotron emissivity spectrum resulting from the power-law distribution of electrons $N_e(\gamma_e) \propto \gamma_e^{-p}$ will then have a peak flux $F_\nu(\nu_p) \propto t^{-2}$ at $\nu_p \propto t^{-4}$, and the self-absorption frequency will decrease with time as $\nu_a \propto t^{-1}$ for $\nu_p < \nu_a$, or $\nu_a \propto t^{-(4p+6)/(p+4)}$ otherwise. In this scenario, the optical frequency must be between the peak of emissivity and the self-absorption cut-off ($\nu_p < \nu_{\text{opt}} < \nu_a$) in order for the predicted optical light curve $F_\nu(\nu_{\text{opt}}) \propto t^3$ to fit the observations. Other possible arrangements of frequencies result in a much slower flux increase $F_\nu(\nu_{\text{opt}}) \propto t$. The “unveiling” of the optical synchrotron peak would occur a few seconds after the corresponding pulse of gamma rays, when the adiabatic expansion of the shocked medium had developed. The model also predicts a very blue optical spectrum $F_\nu \propto \nu^{2.5}$ during the fast initial rise, providing a well-defined observational test.

There is a growing evidence that the basic SSC mechanism is important during the prompt phase of most classical long-duration GRBs. Optically bright bursts detected during the gamma-ray emission, such as GRB 080319B, 990123 and 061126, tend to have a large “excess” of optical light compared to the continuation of the high energy component (Corsi et al. 2005; Perley et al. 2008), consistent with the synchrotron peak falling near or slightly below 2 eV. On the other hand, in two well observed bursts showing faint prompt optical emission (GRB 041219B and 050820A; $F_{\text{opt}}/F_\gamma \sim 10^{-5}$) the implied average optical-to-gamma spectrum is flatter than $\nu^{-1/2}$ and the optical and gamma-ray light curves are closely correlated (Vestrand et al. 2005, 2006). Without additional information, such as the color of the prompt optical light, it is impossible in this case to rule out a single spectral component peaking between 2 eV and 100 keV. However, in both objects the high-energy end of the gamma-ray spectrum follows the optical flux more closely than the low-energy part, as expected in the SSC scenario with the optical band well above the synchrotron peak.

4.2. Transition to afterglow

The parameters of the early fast-decaying component are marginally consistent with the relation $\alpha = 2 + \beta$ expected for large-angle emission that sets the upper limit on the rate of flux decline due to photons emitted at angles larger than $1/\Gamma$ relative to the direction toward the observer (Kumar & Panaitescu 2000). The measurements are harder to reconcile with the reverse shock model (Kobayashi & Sari 2000; Panaitescu & Kumar 2004) that predicts a slower decay with $1.5 < \alpha < 2.0$ for the observed spectrum. This suggests that the early optical afterglow flux arises from the prompt radiation mechanism and that those optical photons arrive at observer later than the burst simply due to a longer photon path from the curved emitting surface to the observer. The contrast generated by exceptionally bright prompt optical signal in GRB 080319B makes it easier to detect large-angle emission from the burst tail that competes with the slower decaying external shock emission. Within the context of the standard fireball model, the transition to a shallower decay after 800 s is most likely associated with the emergence of the forward shock driven by the relativistic ejecta into the circum-burst medium (Meszaros & Rees 1997; Sari et al. 1998). However, assuming a constant color we obtain values α_2 and β_2 that do not fit the standard blast wave solutions for the most likely density profiles r^{-2} (stellar wind) and r^0 (uniform interstellar medium). It is also difficult to explain the X-ray light curve (Racusin et al. 2008b) becoming steeper around 3000 s. At very late times ($\sim 4 \times 10^4$ s) the model with evolving color approaches the closure relation $\alpha = (3\beta + 1)/2$ for a wind medium (Table 1). The data from other instruments point to similar difficulties with the canonical model (Bloom et al. 2008, Racusin et al. 2008c). Racusin et al. (2008c) show that a consistent interpretation of the XRT light curve and the blue color of the slow-decaying component at early times can be achieved by extending the model with an additional strongly collimated outflow (two nested jets), or introducing a complicated density profile in the external medium (local clumps). The specific model fit assuming the second scenario presented by Racusin et al. (2008c) suggests that the cooling break crossed the optical bands ($I \rightarrow R \rightarrow V$) between $t = 150$ and 250 s. This would result in a dramatic change of the spectral slope $\Delta\beta \simeq -0.4$ ($\Delta(V - I) \simeq -0.25$ mag) in just 100 s, contradicting the simultaneous color measurements from RAPTOR-T (Fig. 2). The $(V - R)$ and $(R - I)$ color curves in Fig. 2 do show some structure in excess of the systematic errors near $t \sim 500$ s, but the reality of this feature is uncertain due to coinciding problems with wind-shake. On the other hand, the model fits in Table 1 provide a hint that a separate blue component with the temporal profile similar to the X-ray light curve contributes a modest fraction of the total optical flux near $t \sim 1000$ s, before the slow decaying forward shock emission starts to dominate. Therefore, the RAPTOR data are consistent with the preferred model of Racusin et al. (2008c) comprising a narrow jet (half opening angle $\theta_j \simeq 0.2^\circ$) inside a less collimated outflow ($\theta_j \simeq 4^\circ$), and generating optical emission from forward shocks at

two separate sites.

4.3. Future outlook

The unprecedented panchromatic and temporal coverage of GRB 080319B revealed complexities in both the burst mechanism and the resulting afterglow that are challenging the standard fireball model. Simultaneous multi-color observations in optical/NIR energies during the burst proper are within the reach of the current rapid response telescopes for bright and long-lasting events. With the introduction of even modest spectral capability—such as measuring the sign of the spectral index—the next generation of persistent wide-field sky monitors (Vestrand et al. 2002; Beskin et al. 2008) will provide a solid identification of the burst radiation mechanism and probe its possible diversity.

This research was performed as part of the Thinking Telescopes and RAPTOR projects supported by the Laboratory Directed Research and Development (LDRD) program at LANL.

REFERENCES

- Akerlof, C., et al. 2003, *PASP*, 115, 132
- Beskin, G., et al. 2008, in *AIP Conf. Proc.*, 984, “High Time Resolution Astrophysics: The Universe at Sub-Second Timescales”, ed. D. Phelan, O. Ryan, & A. Shearer, (Melville NY: AIP), 73
- Bloom, J. S., et al. 2008, *ApJ*, in press (astro-ph/0803.3215)
- Blustin, A. J., et al. 2006, *ApJ*, 637, 901
- Boer, M. 2004, *Astron. Nachrichten*, 322, 343
- Corsi, A., et al. 2005, *A&A*, 438, 829 “UV and Gamma-Ray Space Telescope Systems”, eds. G. Hasinger, M. J. L. Turner, 5492, 1613
- Covino, S., et al. 2004, in *Proc. of the SPIE*,
- Ćwiok, M., et al. 2007, *Ap&SS*, 309, 531
- Ćwiok, M., et al. 2008, *GCN Circ.* 7439, <http://gcn.gsfc.nasa.gov/gcn/gcn3/7439.gcn3>

- Gehrels, N., et al. 2004, *ApJ*, 611, 1005
- Golenetskii, S., et al. 2008, GCN Circ. 7482, <http://gcn.gsfc.nasa.gov/gcn/gcn3/7482.gcn3>
- Guidorzi, C., et al. 2006, *PASP*, 118, 288
- Henden, A. 2008, GCN Circ. 7631, <http://gcn.gsfc.nasa.gov/gcn/gcn3/7631.gcn3>
- Karpov, S., et al. 2008, GCN Circ. 7558, <http://gcn.gsfc.nasa.gov/gcn/gcn3/7558.gcn3>
- Kobayashi, S., & Sari, R. 2000, *ApJ*, 542, 819
- Kumar, P., & Panaitescu, A. 2000, *ApJ*, 541, L51
- Meszáros, P., & Rees, M. 1993, *ApJ*, 405, 278
- Meszáros, P., & Rees, M. 1997, *ApJ*, 476, 232
- Panaitescu, A., & Kumar, P. 2004, *MNRAS*, 353, 511
- Panaitescu, A., & Kumar, P. 2007, *MNRAS*, 306, 1065
- Panaitescu, A., & Meszáros, P. 2000, *ApJ*, 544, L17
- Pei, Y. 1992, *ApJ*, 395, 130
- Perley, D. A., et al. 2008, *ApJ*, 672, 449
- Perez-Ramirez, D., Park, H. S., Williams, G. G. 2004, *Astron. Nachrichten*, 325, 667
- Racusin, J. L., et al. 2008a, GCN Circ. 7427, <http://gcn.gsfc.nasa.gov/gcn/gcn3/7427.gcn3>
- Racusin, J. L., et al. 2008b, GCN Circ. 7459, <http://gcn.gsfc.nasa.gov/gcn/gcn3/7459.gcn3>
- Racusin, J. L., et al. 2008c, *Nature*, 455, 183
- Reichert, D. E. et al. 2005, *Nuovo Cimento C Geophysics Space Physics C*, 28, 767
- Rykoff, E. S., et al. 2005, *ApJ*, 631, 121L
- Sakamoto, T. et al. 2008, *ApJS*, 175, 179
- Sari, R., Piran, T., & Narayan, R. 1998, *ApJ*, 497, L17
- Schlegel, D. J., Finkbeiner, D. P., & Davis, M. 1998, *ApJ*, 500, 525
- Vestrand, W. T., et al. 2002, *Proc. SPIE*, 4845, 126

Vestrand, W. T., et al. 2005, *Nature*, 435, 178

Vestrand, W. T., et al. 2006, *Nature*, 442, 172

Vreeswijk, P. M., et al. 2008, *GCN Circ.* 4444, <http://gcn.gsfc.nasa.gov/gcn/gcn3/7444.gcn3>

Waxman, E. 1997, *ApJ*, 485, L5

Woosley, S. E., & Bloom, J. S. 2006, *ARA&A*, 44, 507

Woźniak, P. R., et al. 2004, *AJ*, 127, 2436

Zhang, W., Woosley, S. E., & MacFadyen, A. I. 2003, *ApJ*, 586, 356

Table 1. Multi-color light curve models of GRB 080319B.

α_1	β_1	α_2	β_2	A_V	$d\beta_2/d \log t$	$\chi_\nu^2(\chi^2/\text{dof})$
$2.47^{+0.02}_{-0.02}$	$0.55^{+0.02}_{-0.04}$	$1.15^{+0.01}_{-0.01}$	$0.17^{+0.02}_{-0.06}$	$0.06^{+0.02}_{-0.06}$...	1.04(713.8/687)
$2.45^{+0.02}_{-0.02}$	$0.63^{+0.02}_{-0.04}$	$1.18^{+0.01}_{-0.01}$	$0.22^{+0.02}_{-0.12}$	$0.07^{+0.01}_{-0.07}$	$0.28^{+0.07}_{-0.07}$	0.96(656.3/686)

Note. — The light curve clearly shows small bumps and wiggles that are not captured by the model. Measurement errors were rescaled to achieve $\chi_\nu^2 \sim 1.0$ by adding a systematic uncertainty 0.07 mag to all data points. The value of β_2 in the second model with color evolution corresponds to $t = 10^4$ s.

Table 2. RAPTOR observations of GRB 080319B.

t_{mid} (s)	Δt_{exp} (s)	C_{R} (mag)	V (mag)	R (mag)	I (mag)
RAPTOR-Q					
6.87	10.00	8.412 ± 0.118
37.22	10.00	5.497 ± 0.017
60.48	10.00	6.747 ± 0.035
83.81	10.00	7.943 ± 0.089
RAPTOR-P					
100.31	10.00	8.348 ± 0.020
116.19	10.00	8.758 ± 0.020
132.25	10.00	9.085 ± 0.021
148.22	10.00	9.392 ± 0.021
164.07	10.00	9.591 ± 0.021
179.95	10.00	9.832 ± 0.021
195.98	10.00	9.981 ± 0.022
211.85	10.00	10.151 ± 0.022
228.09	10.00	10.431 ± 0.023
243.72	10.00	10.567 ± 0.024
259.71	10.00	10.715 ± 0.024
275.57	10.00	10.865 ± 0.026
291.53	10.00	11.047 ± 0.028
307.18	10.00	11.248 ± 0.028
323.25	10.00	11.357 ± 0.030
339.30	10.00	11.572 ± 0.035
355.19	10.00	11.576 ± 0.035
370.71	10.00	11.800 ± 0.039
386.57	10.00	11.817 ± 0.039
416.62	30.00	11.965 ± 0.030
456.57	30.00	12.222 ± 0.033
495.99	30.00	12.423 ± 0.038

Table 2—Continued

t_{mid} (s)	Δt_{exp} (s)	C_{R} (mag)	V (mag)	R (mag)	I (mag)
534.69	30.00	12.617 ± 0.043
575.05	30.00	12.699 ± 0.047
614.77	30.00	12.751 ± 0.047
RAPTOR-T					
101.63	10.00	...	8.713 ± 0.020	...	7.991 ± 0.020
114.96	10.00	...	9.052 ± 0.020	8.756 ± 0.020	8.248 ± 0.020
127.89	10.00	...	9.322 ± 0.020	8.981 ± 0.020	8.540 ± 0.020
140.81	10.00	...	9.521 ± 0.020	9.197 ± 0.020	8.739 ± 0.020
153.74	10.00	...	9.717 ± 0.020	9.430 ± 0.020	9.002 ± 0.020
166.66	10.00	...	9.925 ± 0.020	9.609 ± 0.020	9.156 ± 0.020
180.60	10.00	...	10.059 ± 0.020	9.808 ± 0.020	9.318 ± 0.020
193.52	10.00	...	10.230 ± 0.020	9.985 ± 0.020	9.503 ± 0.020
206.25	10.00	...	10.437 ± 0.020	10.140 ± 0.020	9.661 ± 0.020
218.97	10.00	10.250 ± 0.020	10.546 ± 0.020	10.291 ± 0.020	9.869 ± 0.020
231.70	10.00	10.399 ± 0.020	10.723 ± 0.020	10.452 ± 0.020	9.993 ± 0.020
244.43	10.00	10.515 ± 0.020	10.876 ± 0.020	10.568 ± 0.020	10.141 ± 0.020
257.45	10.00	10.637 ± 0.020	11.000 ± 0.020	10.709 ± 0.020	10.286 ± 0.020
270.38	10.00	10.791 ± 0.020	11.116 ± 0.020	10.815 ± 0.020	10.431 ± 0.020
283.30	10.00	10.925 ± 0.020	11.232 ± 0.020	10.971 ± 0.020	10.483 ± 0.020
296.23	10.00	11.053 ± 0.020	11.356 ± 0.020	11.100 ± 0.020	10.623 ± 0.020
309.15	10.00	11.156 ± 0.020	11.519 ± 0.020	11.194 ± 0.020	10.771 ± 0.020
322.08	10.00	11.320 ± 0.020	11.608 ± 0.020	11.333 ± 0.020	10.879 ± 0.020
334.80	10.00	11.409 ± 0.020	11.724 ± 0.020	11.451 ± 0.020	11.030 ± 0.020
360.05	30.00	11.579 ± 0.020	11.914 ± 0.020	11.615 ± 0.020	11.203 ± 0.020
395.50	30.00	11.773 ± 0.020	12.203 ± 0.020	11.878 ± 0.020	11.506 ± 0.020
431.04	30.00	12.046 ± 0.020	12.400 ± 0.020	12.024 ± 0.020	11.670 ± 0.020
466.29	30.00	12.113 ± 0.020	12.542 ± 0.020	12.164 ± 0.020	11.857 ± 0.020
502.44	30.00	12.303 ± 0.020	12.739 ± 0.020	12.343 ± 0.020	12.021 ± 0.021
537.68	30.00	12.484 ± 0.020	12.795 ± 0.020	12.545 ± 0.021	12.129 ± 0.021
573.23	30.00	12.511 ± 0.020	12.956 ± 0.020	12.602 ± 0.021	12.249 ± 0.021

Table 2—Continued

t_{mid} (s)	Δt_{exp} (s)	C_{R} (mag)	V (mag)	R (mag)	I (mag)
608.77	30.00	12.731 ± 0.020	13.060 ± 0.020	12.759 ± 0.021	12.414 ± 0.021
644.32	30.00	12.799 ± 0.020	13.192 ± 0.020	12.838 ± 0.021	12.556 ± 0.021
679.86	30.00	12.904 ± 0.020	13.283 ± 0.020	13.007 ± 0.021	12.599 ± 0.022
715.21	30.00	12.972 ± 0.020	13.304 ± 0.020	13.038 ± 0.021	12.687 ± 0.021
750.45	30.00	13.034 ± 0.020	13.417 ± 0.021	13.141 ± 0.021	12.795 ± 0.022
786.09	30.00	13.185 ± 0.020	13.522 ± 0.021	13.224 ± 0.022	12.856 ± 0.022
821.85	30.00	13.280 ± 0.021	13.576 ± 0.021	13.274 ± 0.022	12.898 ± 0.022
857.39	30.00	13.316 ± 0.021	13.622 ± 0.021	13.371 ± 0.022	13.028 ± 0.022
892.84	30.00	13.413 ± 0.021	13.809 ± 0.021	13.473 ± 0.022	13.131 ± 0.023
928.38	30.00	13.528 ± 0.021	13.823 ± 0.021	13.557 ± 0.022	13.297 ± 0.023
963.52	30.00	13.690 ± 0.021	13.911 ± 0.021	13.681 ± 0.023	13.335 ± 0.024
998.76	30.00	13.744 ± 0.021	13.997 ± 0.021	13.724 ± 0.023	13.318 ± 0.024
1034.51	30.00	13.753 ± 0.021	14.060 ± 0.021	13.836 ± 0.023	13.436 ± 0.024
1070.46	30.00	13.886 ± 0.021	14.157 ± 0.021	13.870 ± 0.023	13.471 ± 0.024
1106.31	30.00	13.914 ± 0.022	14.237 ± 0.022	13.932 ± 0.024	13.610 ± 0.026
1142.56	30.00	13.935 ± 0.022	14.328 ± 0.022	13.973 ± 0.024	13.660 ± 0.026
1177.80	30.00	14.010 ± 0.022	14.391 ± 0.022	14.064 ± 0.024	13.741 ± 0.026
1213.45	30.00	14.156 ± 0.022	14.438 ± 0.023	14.162 ± 0.026	13.802 ± 0.028
1249.20	30.00	14.145 ± 0.022	14.396 ± 0.022	14.179 ± 0.026	13.863 ± 0.028
1284.84	30.00	14.305 ± 0.022	14.520 ± 0.022	14.280 ± 0.026	13.900 ± 0.028
1320.29	30.00	14.277 ± 0.022	14.616 ± 0.023	14.419 ± 0.028	14.030 ± 0.031
1355.93	30.00	14.332 ± 0.022	14.718 ± 0.023	14.328 ± 0.026	14.044 ± 0.030
1391.59	30.00	14.408 ± 0.023	14.683 ± 0.024	14.362 ± 0.028	14.150 ± 0.033
1426.92	30.00	14.455 ± 0.022	14.776 ± 0.023	14.511 ± 0.028	14.139 ± 0.030
1462.27	30.00	14.446 ± 0.023	14.857 ± 0.024	14.535 ± 0.028	14.230 ± 0.031
1497.71	30.00	14.728 ± 0.024	14.891 ± 0.025	14.591 ± 0.032	14.309 ± 0.038
1532.96	30.00	14.614 ± 0.022	14.891 ± 0.023	14.629 ± 0.028	14.315 ± 0.032
1568.30	30.00	14.637 ± 0.024	14.932 ± 0.025	14.735 ± 0.032	14.379 ± 0.037
1603.85	30.00	14.678 ± 0.024	15.012 ± 0.025	14.796 ± 0.034	14.421 ± 0.038
1639.29	30.00	14.734 ± 0.024	15.038 ± 0.025	14.805 ± 0.032	14.537 ± 0.038
1674.64	30.00	14.784 ± 0.025	15.085 ± 0.027	14.886 ± 0.036	14.479 ± 0.041
1710.48	30.00	14.804 ± 0.024	15.082 ± 0.026	14.927 ± 0.034	14.623 ± 0.040

Table 2—Continued

t_{mid} (s)	Δt_{exp} (s)	C_{R} (mag)	V (mag)	R (mag)	I (mag)
1745.83	30.00	14.808 ± 0.024	15.156 ± 0.026	14.895 ± 0.034	14.594 ± 0.039
1780.96	30.00	14.932 ± 0.026	15.229 ± 0.028	15.061 ± 0.039	14.750 ± 0.047
1816.52	30.00	15.003 ± 0.024	15.263 ± 0.026	14.966 ± 0.034	14.715 ± 0.041
1852.06	30.00	15.028 ± 0.026	15.274 ± 0.028	15.019 ± 0.037	14.666 ± 0.043
1887.61	30.00	14.996 ± 0.028	15.269 ± 0.029	14.994 ± 0.039	14.774 ± 0.049
1923.25	30.00	15.004 ± 0.027	15.342 ± 0.030	15.209 ± 0.043	14.726 ± 0.047
1958.70	30.00	15.046 ± 0.028	15.352 ± 0.030	15.073 ± 0.041	14.832 ± 0.053
1993.94	30.00	15.079 ± 0.026	15.443 ± 0.028	15.143 ± 0.039	14.882 ± 0.047
2029.29	30.00	15.176 ± 0.028	15.333 ± 0.030	15.197 ± 0.044	14.889 ± 0.055
2064.93	30.00	15.157 ± 0.025	15.457 ± 0.028	15.182 ± 0.036	14.954 ± 0.048
2100.88	30.00	15.188 ± 0.028	15.455 ± 0.031	15.371 ± 0.047	14.925 ± 0.052
2136.02	30.00	15.222 ± 0.028	15.403 ± 0.029	15.268 ± 0.042	14.965 ± 0.052
2171.37	30.00	15.294 ± 0.028	15.477 ± 0.030	15.338 ± 0.044	14.858 ± 0.048
2224.64	150.00	15.229 ± 0.024	15.516 ± 0.025	15.330 ± 0.031	14.985 ± 0.035
2401.79	150.00	15.379 ± 0.025	15.680 ± 0.027	15.479 ± 0.034	15.139 ± 0.041
2667.83	300.00	15.549 ± 0.023	15.884 ± 0.024	15.593 ± 0.028	15.281 ± 0.033
3023.57	300.00	15.828 ± 0.024	16.044 ± 0.025	15.799 ± 0.031	15.537 ± 0.039
3379.09	300.00	15.934 ± 0.025	16.227 ± 0.027	15.989 ± 0.034	15.625 ± 0.042
3734.19	300.00	15.981 ± 0.026	16.306 ± 0.028	16.071 ± 0.037	15.822 ± 0.047
4265.78	600.00	16.260 ± 0.024	16.471 ± 0.025	16.260 ± 0.032	15.965 ± 0.039
4976.18	600.00	16.407 ± 0.026	16.763 ± 0.028	16.496 ± 0.036	16.151 ± 0.046
5686.59	600.00	16.660 ± 0.027	16.930 ± 0.030	16.661 ± 0.040	16.322 ± 0.050
6396.62	600.00	16.780 ± 0.028	17.046 ± 0.030	16.853 ± 0.043	16.635 ± 0.064

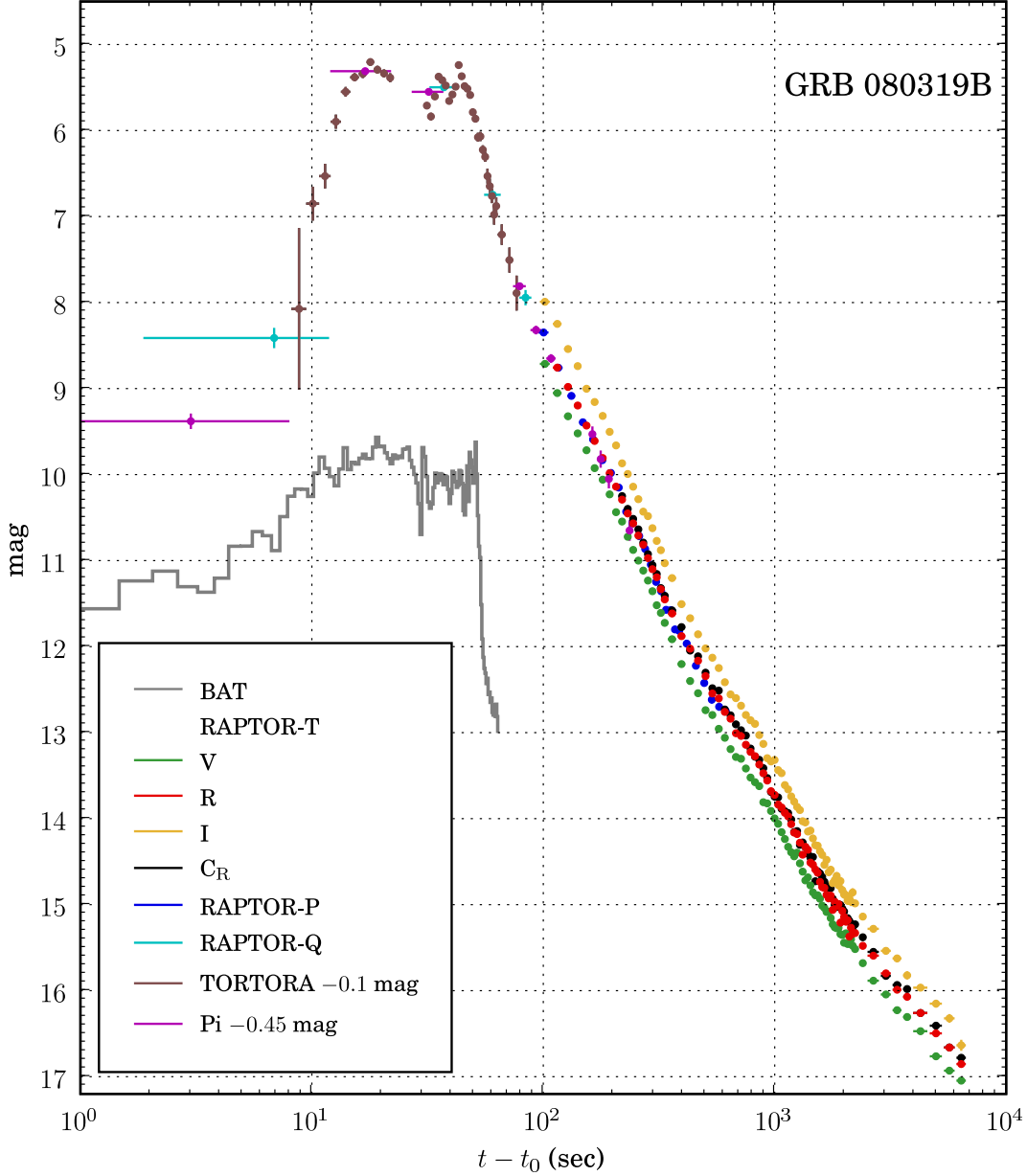


Fig. 1.— Optical light curve of GRB 080319B, “the naked eye burst”. The transient was independently detected and followed over a high dynamic range by three fully autonomous instruments on the RAPTOR telescope network: a simultaneous multi-color imager RAPTOR-T, a wide-field survey array RAPTOR-P, and an all-sky monitor RAPTOR-Q. A non-detection in RAPTOR-Q data rules out the presence of a significant optical precursor for ~ 30 minutes prior to BAT trigger at t_0 . The RAPTOR measurements of the prompt optical emission during the gamma-ray burst ($t - t_0 = 0 - 60$ s.) agree with the data collected by other instruments reporting detections: TORTORA (Karpov et al. 2008) and Pi-of-the-sky (Ćwiok et al. 2008). Unfiltered observations were adjusted to R -band equivalent scale.

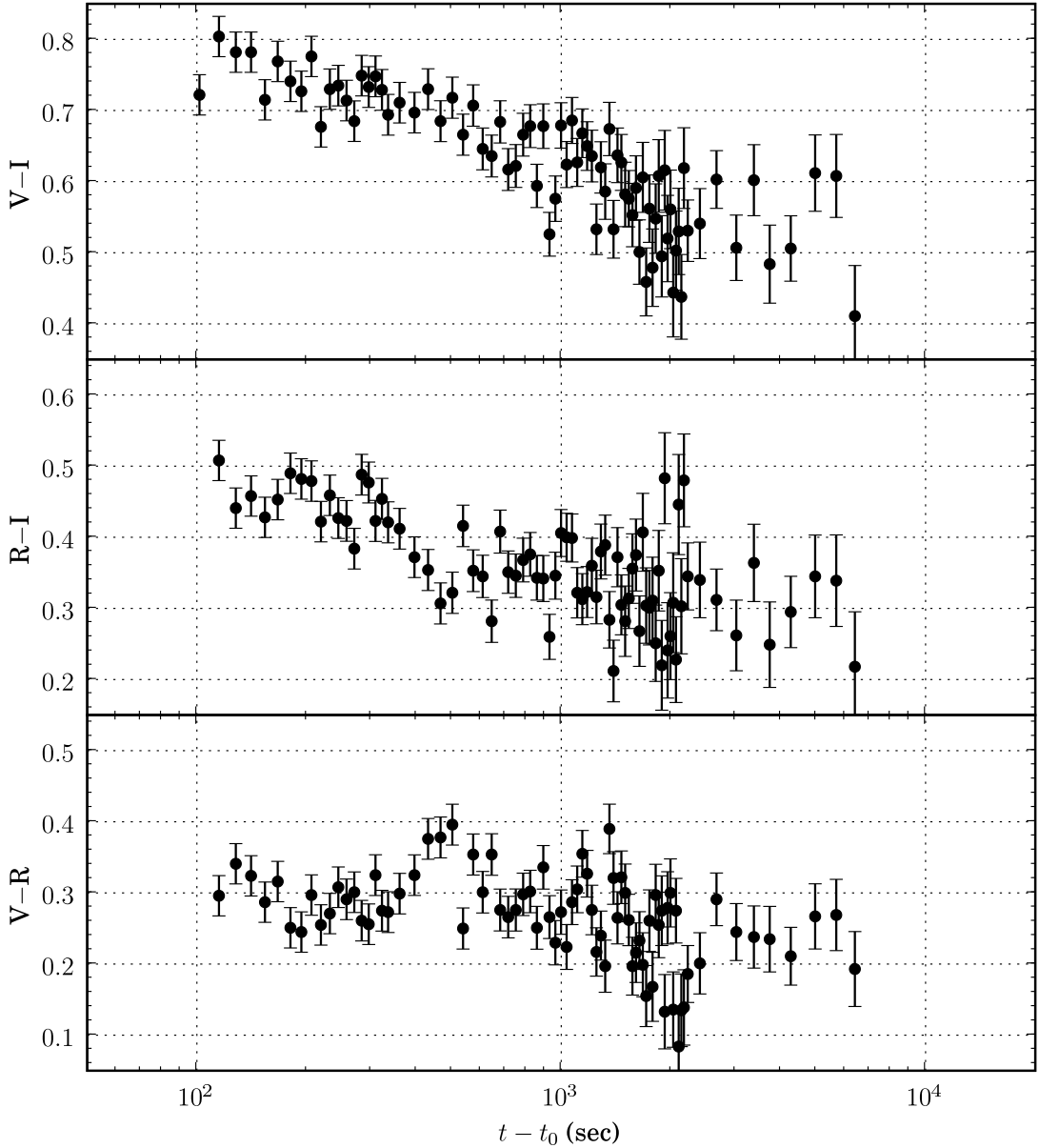


Fig. 2.— Color evolution of the optical afterflow of GRB 080319B. The simultaneous multi-color measurements collected by RAPTOR-T show that the apparent color of the optical transient gradually evolves from $(V - I) \simeq 0.80$ at 100 s toward a much bluer value $(V - I) \simeq 0.55$ around 2000 s, and then remains approximately constant until 6500 s. There is no indication of short time-scale variability in color despite the presence of several bumps in the light curve that modulate smoothly decaying afterglow flux by about 10% on time-scales 100–300 s.

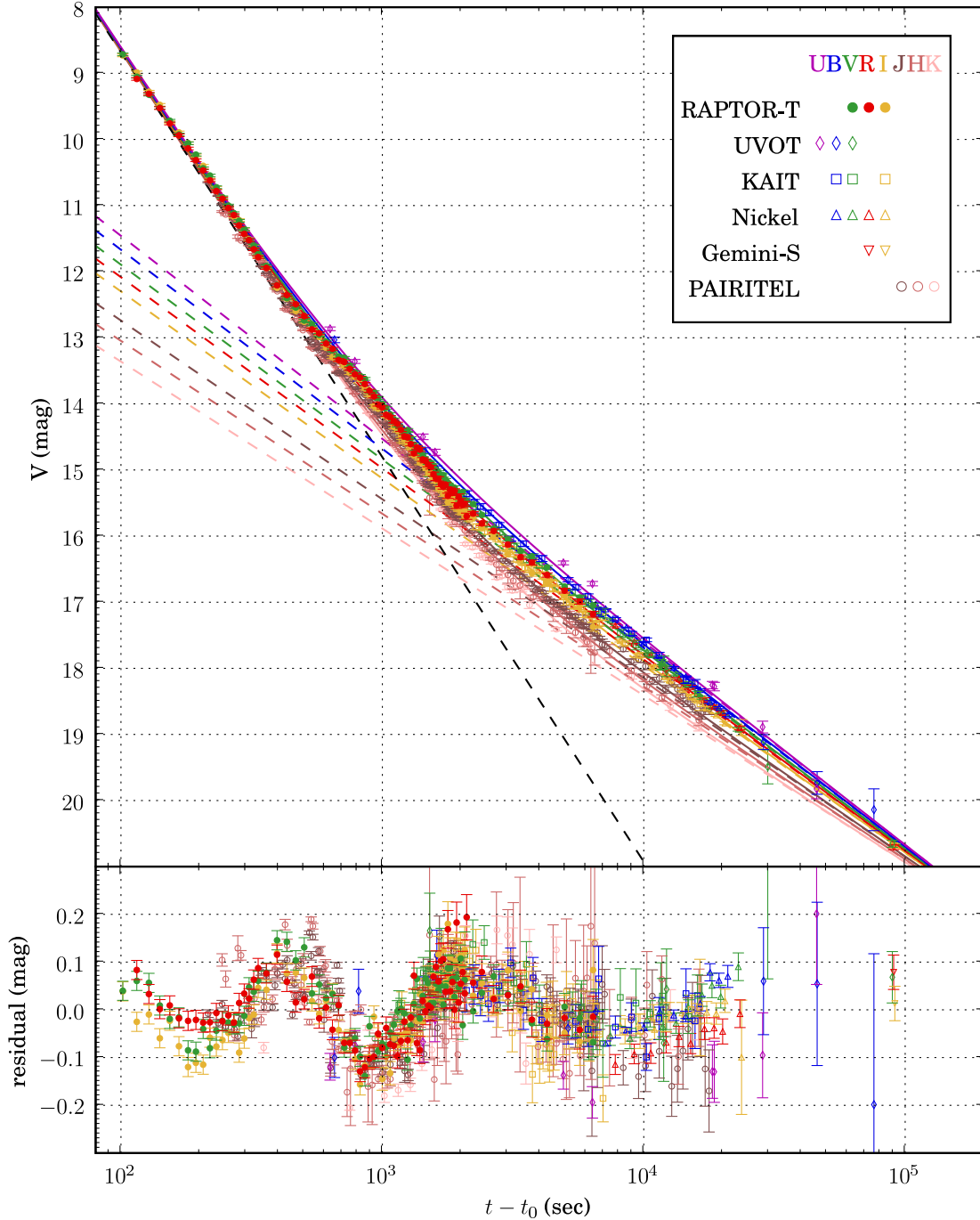


Fig. 3.— Optical and NIR light curves of the GRB 080319B afterglow. The simultaneous multi-color RAPTOR-T measurements are compared to data from other instruments (Bloom et al. (2008)). The lines show the best fit model with color evolution from Table 1. Dashed lines are for individual components and solid lines are the totals in each filter. The measurements and the model fits in all photometric bands were shifted to absorb the constant color of the early fast-decaying component using the V band as reference.

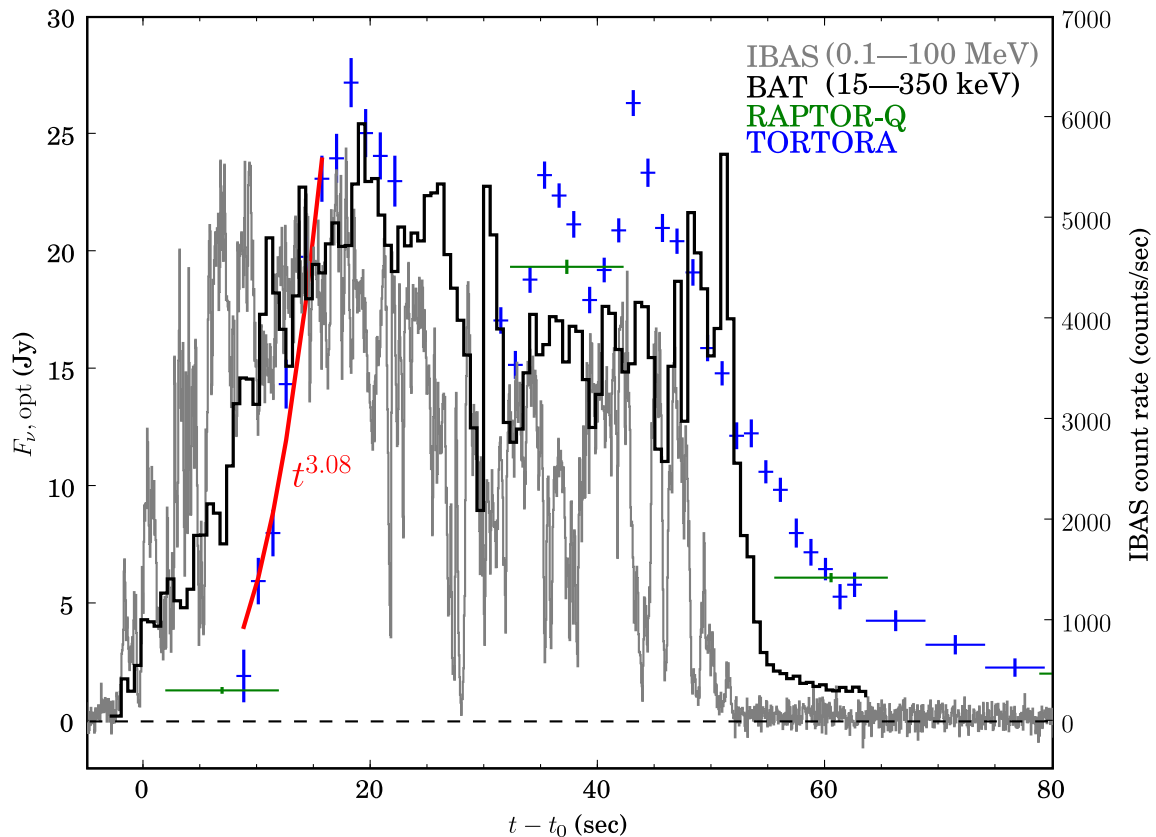


Fig. 4.— A comparison of the prompt optical light curve and the hard X-ray to gamma-ray light curve of GRB 080319B. The average gamma-ray flux shows a gradual rise to the peak value and is accompanied by extremely rapid onset $\sim t^3$ of very strong prompt optical emission. In the synchrotron self-Compton scenario the synchrotron spectrum peaking near the optical frequency window is initially suppressed by self-absorption. The expanding fireball quickly becomes optically thin at low energies allowing photons near the peak of synchrotron emissivity to escape.